arXiv:0908.2433v1 [astro-ph.HE] 17 Aug 2009

Draft as of August 17, 2009.

RHESSI Tests of Quasi-Thermal Gamma-Ray Burst Spectral Models

Eric C. Bellm[1,2]

ABSTRACT

Prompt gamma-ray burst spectra evolve on short time scales, suggesting that time-resolved spectral fits may help diagnose the still unknown prompt emission mechanism. We use broad-band gamma-ray data from the RHESSI spacecraft to test quasi-thermal models with high signal-to-noise time-resolved spectra of nine bright gamma-ray bursts. In contrast to results reported in more narrow energy bands, the quality of the fits of quasi-thermal models is poor in relation to fits of the phenomenological Band function. Moreover, the best-fit parameters for the simplest quasi-thermal model, a black body plus a nonthermal power law, show significant dependence on the fit band. Models that replace the power law with more complicated nonthermal functions are not robust for the data considered here and decrease the physical relevance of the fit black body.

Subject headings: gamma-rays: bursts

1. Introduction

One of the most distinct features of the initial gamma-ray emission of gamma-ray bursts (GRBs) is its temporal variability. Significant evolution of the lightcurve and the spectrum occurs on timescales shorter than the total burst duration. Accordingly, spectral fits of subintervals of a burst may provide improved insight into the burst emission mechanism, at the cost of increased complexity.

When the Band et al. (1993) phenomenological spectral model (the "Band function", a smoothly connected broken power law) was found to successfully fit the GRB prompt

[1]UC Berkeley Space Sciences Laboratory, 7 Gauss Way, Berkeley, CA 94720-7450, USA

[2]ebellm@ssl.berkeley.edu

emission observed by BATSE, systematic time-resolved analyses of large burst samples focused on identifying patterns in the fit parameter evolution in an attempt to gain insight into the emission mechanism of long GRBs. Ford et al. (1995), Crider et al. (1997), and Preece et al. (1998b) considered the evolution of the peak energy E_{peak}, low-energy power-law index α, and high-energy power-law index β, respectively. Broadly, these authors found a typical hard-to-soft decay of the emission and a general correlation of spectral hardness with intensity.

The observation of hard low-energy spectral slopes ($\alpha \sim +1$) in the initial portions of GRB pulses raised concerns about the viability of the synchrotron shock model, as $\alpha > -2/3$ violated the "line of death" for optically thin synchrotron (OTS) emission (Crider et al. 1997; Preece et al. 1998a; Ghirlanda et al. 2002; Preece et al. 2002). These violations, in concert with theoretical expectations from the fireball model (e.g., Mészáros & Rees 2000), led authors to suggest such emission could have a thermal origin (Crider et al. 1997; Preece 2000). Ghirlanda et al. (2003) found that time-resolved BATSE LAD spectra with hard low-energy indices could be acceptably fit with a black-body spectrum. This result was confirmed by Ryde (2004) for hard, single pulses. In some cases the addition of a simple power-law improved the correspondence with the high-energy LAD data. These successes led Ryde (2005) to propose that all GRB emission might be decomposed into thermal and nonthermal components of similar magnitude, with the black-body emission providing the spectral peak of the prompt emission. Within the LAD band, a simple power law proved a sufficient approximation to the more complicated true nonthermal emission, with the resulting black-body plus power-law model (BBPL) fits having similar χ^2 values as the Band function for identical degrees of freedom. In Ryde et al. (2006), the authors noted that the power-law slope of the BBPL model avoided the OTS line of death and sought to interpret the black body fit results in the context of a photospheric model. Most recently, Ryde & Pe'er (2008) (hereafter, RP08) identified regularity in the time evolution of the temperature and flux of the black-body component for single-pulse bursts and linked the normalization of the black-body component to the size of the thermal emitting region (see also Pe'er et al. 2007).

While the simple power-law approximating the nonthermal emission in the BBPL model is effective over the moderate energy band (28 keV–1.8 MeV) of the BATSE LAD detectors, tests of the BBPL model using data covering a broader bandpass have had mixed results. McBreen et al. (2006) successfully fit the BBPL model to GRB 041219A data from *INTEGRAL*-SPI spanning the range 20 keV–8 MeV, although the black body contributed only a small portion of the flux of the main burst. Foley et al. (2008) obtained acceptable time-integrated fits of the BBPL model to GRBs observed by *INTEGRAL*-IBIS and SPI, although the IBIS detection requirement created a burst sample with relatively low peak spectral energies ($E_{peak} <\sim 150$ keV). Ghirlanda et al. (2007) considered BATSE bursts co-

observed in the X-ray by the Beppo-SAX WFC. Time-resolved spectra were not available for the WFC data, but a summation of the time-resolved BBPL fits to the BATSE data led to a significant overprediction of the WFC flux, while a similar extrapolation of the summed time-resolved Band function fits was much more successful.

In this work, we have employed data from the Ramaty High Energy Solar Spectroscopic Imager (RHESSI) (Lin et al. 2002) to investigate the behavior of quasithermal spectral models over a broad energy band. RHESSI's nine coaxial germanium detectors image the Sun at X-ray to gamma-ray energies (3 keV–17 MeV) with excellent resolution in energy (1–5 keV) and time (1 binary μs) (Smith et al. 2002). RHESSI's detectors are effectively unshielded above $\sim$30 keV and receive emission from astrophysical sources like GRBs with a total effective area of $\sim$150 cm^2. Each coaxial detector is electronically segmented into thin front and thick rear segments; most off-axis emission is recorded in the rear segments. The satellite rotates with a period of about 4 seconds.

2. Data Analysis

2.1. Sample Selection

The identification of optimal fit intervals for time-resolved spectral fitting requires balancing the need for high signal-to-noise (in order to constrain the fit parameters of the spectral models) with the goal of the finest possible time resolution. In our previous systematic analysis of RHESSI GRBs (Bellm et al. 2008), we found that a S/N ratio of at least 45 was required for adequate fitting of the most complicated models. This value is also consistent with those adopted by previous studies of time-resolved BATSE spectra (Crider et al. 1997; Kaneko et al. 2006).

Because bursts may have periods of high signal which are degraded to low S/N when integrated over the whole burst, we chose candidate bursts from the RHESSI sample[1] with localizations and total S/N > 30. Radiation damage to RHESSI's germanium detectors has slowly degraded spectral performance; we restricted our analysis to detectors which do not show signs of radiation damage. We therefore considered bursts from the RHESSI launch in February 2002 through June 2006, after which all nine RHESSI detectors were damaged. Forty-five GRBs met these criteria.

To identify subintervals within each candidate burst, we used the Bayesian Blocks algo-

[1] `http://grb.web.psi.ch/`

rithm (Scargle 1998), which identifies the most probable segmentation of a burst lightcurve into intervals of constant Poisson rate. We modified the stopping criterion to generate subintervals of appropriate S/N. Since the RHESSI data are stored event by event, this "top-down" identification of the burst subintervals is more natural than building up data accumulated on fixed timescales until a minimum S/N is reached. While previous work on quasi-thermal models has focused on spectral evolution within pulses, our segmentation method does not require pulse modeling. This approach was necessary, as the bright bursts in this sample generally have irregular temporal structure, but it also avoids imposing additional implicit selection effects on the burst sample.

We applied the Bayesian Blocks algorithm to the raw RHESSI eventlist to identify the most probable segmentation points. The time variation of the background, while present, does not dominate the GRB variability. In our modified stopping criterion, we computed the background-subtracted S/N (in the 60 keV–3 MeV band) for each proposed subinterval. If the S/N ratios of both subintervals were greater than 15, the segmentation was allowed. For each subinterval, we applied the Bayesian Blocks algorithm again if the S/N of that interval was greater than 45. After segmentation halted, we dropped any leading or trailing subintervals with S/N < 45 and combined any "interior" subintervals with low S/N with the adjacent subinterval with lower S/N. The resulting subintervals all have S/N > 45. We conducted spectral fitting only on bursts with at least three subintervals.

The resulting burst sample consists of nine bursts and a total of 88 subintervals. Table 1 lists the bursts and intervals considered in this work. Figure 1 shows the distribution of subinterval length and S/N. These bursts are predominantly from early in the RHESSI mission because for those bursts a greater number of the detectors remained unaffected by radiation damage.

In order to investigate the spectral evolution of single GRB pulses in Section 4.3, it was necessary to set a lower S/N threshold. We used our modified Bayesian Blocks routine to identify subintervals with S/N > 25 within single, separated pulses. This "single-pulse" sample yielded 25 subintervals within 3 GRBs (Table 1).

2.2. Spectral Fitting

2.2.1. Fit Methods

The RHESSI data were extracted in SSW-IDL[2]. We fit a third-order polynomial to background intervals immediately before and after the burst, allowing for a potential periodic modulation of the background with the RHESSI rotation. We selected energy binning for the spectra by requiring at least ten counts in each bin of the raw source spectrum. We used the same energy bins for all subintervals of each burst. Both the source and background spectra covered the energy range 30 keV–17 MeV.

We determined RHESSI's spectral response by simulating monoenergetic photons impinging on a detailed mass model in the Monte Carlo suite MGEANT (Sturner et al. 2000). For a grid of angles relative to the spacecraft rotation axis, we simulated photons along 60° arcs in rotation angle. After interpolating to the appropriate off-axis angle, we weighted the 60° sector responses by the burst light curve to generate the total response. Since many of the subintervals considered in this work were shorter than one-sixth of RHESSI's four second rotation period, responses for short intervals were often single sector responses. Our simulations indicate that the spectral response does not vary appreciably on shorter scales in rotation angle.

We utilized ISIS v1.4.9 (Houck & Denicola 2000) for spectral fitting. Fitting was automated via an ISIS script and the results stored in a database.

We used data from the RHESSI rear segments only for all bursts except for GRBs 021206 and 021008A, which had off-axis angles small enough (18° and 50°, respectively) that appreciable counts were recorded in the front segments. (Coincidentally, these bursts also both had data decimation in the rear segments—only a fraction of the observed counts were recorded.) The fit energy band was 30 keV–17 MeV, with some exceptions: GRB 021206 had significant atmospheric backscatter in the rear segments (Wigger et al. 2008), so the front and rear segment data were kept separate and fit over the range 30 keV–2800 keV and 300 keV–17 MeV. (For all other bursts, data from all detectors were combined into a single spectrum.) GRBs 030519B and 040228 came through the extreme rear of the RHESSI cryostat (166° and 163°), where the low-energy response is more sensitive to the detailed mass modelling, so a fit range of 50 keV–17 MeV was employed. Finally, GRB 021008A required a fit band of 100 keV–17 MeV for adequate fitting; Wigger et al. (2008) found similar behavior in a time-integrated fit of this data.

[2]`http://www.lmsal.com/solarsoft/`

2.2.2. Spectral Models

We fit both the time-resolved and the time-integrated spectra with a variety of spectral models commonly used to represent the GRB prompt emission. The Band function (Band) is a phenomenological model which fits the vast majority of broadband prompt spectra (Band et al. 1993). It is a broken power law with a smooth transition between the upper and lower power laws:

$$N_E = \begin{cases} A(E/E_{piv})^{\alpha} \exp(-E(2+\alpha)/E_{peak}) & E < E_{break} \\ B(E/E_{piv})^{\beta} & E > E_{break} \end{cases} \quad (1)$$

with $E_{break} \equiv E_0(\alpha - \beta)$ and $B \equiv A(\frac{(\alpha-\beta)E_0}{E_{piv}})^{\alpha-\beta} \exp(\beta - \alpha)$. For $\beta < -2$ and $\alpha > -2$, E_{peak} corresponds to the peak of the νF_ν spectrum. The normalization A has units of photons cm^{-2} s^{-1} keV^{-1}, and E_{piv} is here taken to be 100 keV.

While the Band function is often assumed to be the "true" spectral model in fits of GRB spectra, data obtained over a more limited energy band or at lower S/N may not be sufficient to constrain its parameters. We also tested other empirical models with fewer free parameters. The cutoff power law (CPL) is equivalent to the Band function below E_{break}:

$$N_E = A(E/E_{piv})^{\alpha} \exp(-E(2+\alpha)/E_{peak}) \quad (2)$$

We also fit a single power law (PL): $N_E = A(E/E_{piv})^{\alpha}$. While the PL model was a poor fit to these spectra, its fit spectral index was useful in comparison with the other models.

The simplest quasi-thermal spectral model is a black body plus power law model (BBPL). Proposed by Ryde (2005), it consists of Planck function and a simple power law:

$$N_E = A\frac{(E/E_{piv})^2}{\exp E/kT - 1} + B(E/E_{piv})^s \quad (3)$$

The approximation of the nonthermal emission by a simple power-law is an approximation which is generally sufficient over the BATSE energy band (Ryde 2005). However, it is not expected to fit over a broader band (Ryde 2004, 2005; Ryde & Pe'er 2008). Like the PL model, it diverges unphysically.

More sophisticated quasi-thermal models replace the nonthermal PL in the BBPL with an empirical function with more free parameters. We attempt to fit a black body plus cutoff power law (BBCPL) model as well:

$$N_E = A\frac{(E/E_{piv})^2}{\exp E/kT - 1} + B(E/E_{piv})^{\alpha}\exp(-E(2+\alpha)/E_{peak}) \quad (4)$$

(We retain the notation of E_{peak} for the cutoff parameter of the BBCPL model for clarity of comparison, but in some cases the true peak of the νF_ν spectrum may be due to the black-body component at 3.92 kT.) However, the addition of more free fit parameters leads to convergence problems even with our relatively high S/N broad-band spectra. In addition to the unconstrained fits of the BBCPL model, then, we also perform fits in which the variation of the model temperature is constrained to an expected range. We describe the specifics of this constrained quasi-thermal model in the text below.

Given the convergence problems faced by the BBCPL model, we have not attempted fits of a black body + Band model, which contains an additional free parameter. In most cases, the simple CPL model provides an adequate representation of the RHESSI data, with the Band model offering only moderate improvements. Accordingly, the BBCPL model should provide a sufficient test of the importance of the black-body component over the RHESSI band.

3. Fit Results

We present the time-evolution of the fit parameters of the Band and BBPL models in Figures 2–10. The quality of the fits and the constraint of their parameters were generally good. For GRB 021206, the goodness of fit was poorer for some subintervals because of the separation of front and rear data. Slight offsets in the background subtraction created disagreements about the overall model normalization and increased the χ^2. We elected to take the averaged fluence value produced by the fit rather than introduce a fit normalization offset between the front and rear data for this burst. For GRB 021008A, the only other burst with front segment data, our combination of front and rear segment spectra averaged out such background subtraction problems and obviated the need for such offsets.

Wigger et al. (2008) fit RHESSI data for many of these bright bursts using an identical mass model but independent analysis and fit procedures. Our fits of the total burst intervals are a good match to those results (Table 2). In the case of GRB 021206, the presence of excess high-energy emission not well-modeled by the Band function increased the χ^2 value for the fit to 17 MeV. (This component likely also contributed to the poor goodness of fit for this burst in the time-resolved fits, as discussed above, although its impact is harder to ascertain.) *HETE*-2 also observed three bursts in this sample. RHESSI fit higher E_{peak} values for all three bursts; in two of the cases, the peak energies were above the 400 keV

upper bound of the *HETE* energy band.

The distributions of our best-fit parameters are in general agreement with the BATSE results obtained by Kaneko et al. (2006). For our time-resolved Band function fits, the mean α is -1.00 with standard deviation 0.47 (Figure 14). The RHESSI mean E_{peak} is 580 $\pm$ 280 keV, and β has mean -3.50 and standard deviation 0.89. The BATSE results for all good Band fits are $\alpha = -0.90^{+0.34}_{-0.39}$, $E_{peak} = 268^{+188}_{-145}$ keV, and $\beta = -2.33^{+0.39}_{-0.47}$, where we have converted the quartile dispersions to 1σ uncertainties under the simplifying assumption of an underlying normal distribution. Using Levene's test, we find that the variences of the BATSE and RHESSI distributions are consistent. Since the RHESSI distributions are not normal, we cannot compare the means using Student's t-test. The nonparametric Kolmogorov-Smirnov test rejects the null hypothesis BATSE and RHESSI parameter samples are drawn from the same distribution. However, this result is not surprising, given the different fit energy ranges and the few RHESSI bursts fit here. Of the three parameters, the alpha distributions are most consistent despite the apparent bimodality of the RHESSI sample (Fig. 14).

4. Evaluating Quasithermal Models

We did not attempt to determine the best-fit model for each spectrum fit in this work. With the exception of the Band function and the BBPL, the models fit herein have different numbers of fit parameters. As discussed by Protassov et al. (2002), the conventionally used F-test of an additional term is inappropriate if the models being compared are not nested (i.e. the fit parameters of the parsimonious model are not a subset of the more complex model). The rigorous alternative—Bayesian hypothesis testing—would require numerical marginalization over our fit parameters and hence a major reworking of our analysis procedures. Instead, we have opted to evaluate the effectiveness of the quasi-thermal models in three ways: first, by directly comparing goodness-of-fit for those pairs of quasi-thermal and empirical models with identical degrees of freedom; second, by assessing the physical plausibility of the model fits; and third, by considering the robustness of the fits and their relative consistency with each other and previous work.

4.1. BBPL

We begin by considering the simplest quasi-thermal model, the black body + simple power law (BBPL). This model is not expected to be effective over a broad energy band (e.g., Ryde 2005; Ghirlanda et al. 2007). It is instructive to ask, however, how the properties of the

BBPL fits change when fit over a broader band. In particular, evidence of band-dependence calls into question the universality of results obtained even in a narrow band centered on the peak of the prompt emission.

The Band and BBPL models each have four fit parameters (α, E_{peak}, β, and the normalization for Band; kT, s, and the two normalizations for the BBPL). Comparing their χ^2 values for each subinterval (see Fig. 11), we find that in 73 of 88 cases, the Band function has a lower χ^2 value and is thus statistically favored.

As in previous studies, we found that the peak of the blackbody emission (3.92 kT) in BBPL fits corresponded closely to the value of E_{peak} obtained in Band fits (Figure 12b). Moreover, the contribution of the BBPL black-body flux to the overall flux in the band was significant (Figure 13).

Contrary to our expectation, we did not find systematic deviation in the residuals of the fit BBPL model at low or high energy. Such deviation would be symptomatic of the need for additional spectral components (e.g., Ryde & Pe'er 2008).

RHESSI's broader energy band did affect the best-fit value of s, the power law index of the BBPL model. The distribution of s reported by Ryde et al. (2006) peaks around -1.5, while our histogram of s peaks near -1.9 (Fig. 14). This shift may be due to the small sample of bursts fit here, although as discussed in Section 3 the fit Band index α shows only a small shift compared to the BATSE sample.

However, a softer fit index is expected when fitting a power law to GRB data extending to higher energies, as GRB spectra generically fall off more sharply above E_{peak}. The fit single power law index is thus a band-dependent average of the more complicated spectral shape. Indeed, the distribution of s obtained is quite similar to that of the index of a simple power-law fit to these data (Figure 14), and s is highly correlated with the fit PL index for individual intervals. Since the asymptotic spectral index must be greater than -2 below the peak energy and less than -2 above it, fitting a power law to a band of sufficient width which includes the peak energy will average to an intermediate value.

One of the strengths of the BBPL model is that its nonthermal component typically is softer than the "line of death" of $-2/3$ predicted for optically thin synchrotron emission. However, this argument appears to be weakened by the sensitivity of the fit power-law index to the range of the data above the peak energy. It is not clear that the fit value of s provides useful insight into the nonthermal emission physics, as its value may be an artifact of the fit band.

4.2. BBCPL and Variants

Given the challenges faced by the BBPL model in the RHESSI band, we tried more complicated nonthermal components in an attempt to find a functional broad-band quasithermal model. We sought to evaluate the efficacy and robustness of such models and to assess whether the thermal component retained physical relevance and realism.

After a simple power-law, the cutoff-power law (CPL) model is the next most basic nonthermal model. Unlike the PL model, it has the advantage of providing a generally adequate representation of the RHESSI data considered here over the full band. Accordingly, we tested a black-body plus cutoff power law (BBCPL) model.

Given the success of the basic CPL model at fitting these data, it is perhaps not surprising that the CPL component of the BBCPL model dominates the fits. Figure 12c shows that the E_{peak} of the BBCPL fits closely corresponds to the peak energy fit by the Band function. The peak energy of the black-body component alone, however, is almost completely uncorrelated with the peak energy of the phenomenological models (Figures 12d–f). This behavior is in marked contrast to the success of the BBPL model of identifying the spectral peak with the black-body peak. Moreover, many of the fit values of kT in the BBCPL model are limits only, indicating the lack of robustness in the fits.

The bolometric black-body flux is obtained by integrating the differential energy spectrum of the Planck function EN_E over all energies; it equals $A(kT)^4 E_{piv}^2 \pi^4/15$. Its value is fairly similar for the BBPL and BBCPL models. However, since the best-fit black-body temperature is often near the limits of the RHESSI band, the fraction of the flux in the RHESSI band provided by the black body drops sharply in the BBCPL model (Figure 13). The black-body component is accordingly of less relevance in explaining the observed data.

Following Ghirlanda et al. (2007), we also attempted "constrained" fits of the BBCPL model in an attempt to force the black-body component to provide the peak of the spectral emission. We fit a BBCPL model with the black-body peak energy (3.92 kT) constrained to lie within the 90% confidence limit of the best-fit Band E_{peak} value.[3] As expected, the χ^2 value for the constrained BBCPL fits increases dramatically relative to the BBCPL fits, and the best-fit kT value typically does not have 90% confidence limits within the allowed band. The black-body contribution to the total flux in the RHESSI band is not significantly different than for the regular BBCPL model and remains small.

[3]Our approach is less restrictive than that of Ghirlanda et al. (2007), who fixed the black-body peak at E_{peak}.

4.3. Time Evolution

One of the most notable features of the BATSE BBPL fits presented by RP08 is the remarkably universal behavior of the time evolution obtained in the BBPL fits. For their sample of single-pulse bursts, they found that both the fit black-body temperature and the bolometric black-body flux exhibit a regular power law rise and decay. They found identical break times for the flux and temperature evolution in a given burst. Moreover, a dimensionless proxy for the black-body normalization, $\mathcal{R}(t) \equiv (F_{BB}/\sigma T^4)^{1/2} = 1.01 \times 10^{-16} A^{1/2} E_{piv}^{-1}$, is related to the size of the photospheric emission region and increases monotonically even for bursts with complex light curves.

We consider the time evolution of the black-body components of the RHESSI BBPL and BBCPL fits in an attempt to reproduce these behaviors. Since the RP08 time-evolution results were obtained from bursts with simple single-pulse time profiles, we used a single-pulse burst sample with slightly lower signal-to-noise ratio than our high S/N sample of mostly complex bursts. Unfortunately, only 3 bursts met the selection criteria described in Section 2.1. These bursts, GRBs 020715, 030329A, and 060805B, have 8, 12, and 5 subintervals, respectively. Accordingly, caveats of small sample size and limited time resolution apply to our analysis of their time evolution.

We plot the time evolution of the temperature, bolometric black-body flux, and $\mathcal{R}(t)$ in log-log space in Figures 15, 16, and 17. Within the moderate time resolution of these data, there is a clear suggestion of the correlated power-law rise, break, and decay of the temperature and black-body flux for the BBPL model, as found by RP08.

For these three bursts, the BBPL $\mathcal{R}(t)$ values are generally consistent with a constant value. While a minority of the RP08 sample showed such behavior, far more frequently the RP08 bursts had $\mathcal{R}(t)$ values which increased as a power-law over an order of magnitude. The authors interpreted this increase in terms of the expansion of the photospheric emission region. RP08 also found frequent monotonic increases in $\mathcal{R}$ for bursts with complex lightcurves. Our high S/N sample, consisting primarily of bursts with such lightcurves, also all have $\mathcal{R}(t)$ consistent with a constant. The values of $\mathcal{R}$ we obtain are consistent with the RP08 sample, however. Both the single-peak and the high S/N samples range from 7×10^{-20}–2×10^{-18} and peak near 3×10^{-19}.

The time evolution of the BBCPL black body exhibits few clear trends, as expected given the black body's convergence problems and minimal contribution to the fit. For the single-pulse sample, the bolometric black-body flux seems to track that obtained in the BBPL model (Figures 15–17). There is less correlation between the temperatures of the two models, though, and the time evolution of $\mathcal{R}(t)$ for both the single-pulse sample and the

high S/N sample shows little temporal regularity. Moreover, the BBCPL $\mathcal{R}(t)$ value can be more than an order of magnitude different than that obtained in the BBPL fits, ranging from 10^{-23}–10^{-17}. Such changes would imply orders of magnitude change in the inferred size of photospheric emission region, casting further doubt on the physical significance of the black-body component of our BBCPL fits.

5. Conclusions

We have tested quasi-thermal spectral models of GRB prompt emission over a broader energy band (30 keV–17 MeV) than previously considered. Many of the successes of the BBPL model in the BATSE band (acceptable χ^2_ν, physical spectral slopes for the nonthermal component, universal time evolution) are not reproduced consistently in the RHESSI data considered here. We have attempted to construct more realistic quasi-thermal models by combining a black body with a cutoff power-law (BBCPL). However, even using our intervals selected for high quality (S/N$>$ 45), the BBCPL model exhibits convergence difficulties. More crucially, though, the fit black-body component loses its relevance as the origin of the spectral peak. It is possible that bursts with simpler light curves might exhibit better fit behavior or that data obtained over an even wider energy band could clarify the transitions between thermal and nonthermal emission. Data from *Fermi*-GBM and LAT will provide useful tests. However, results from GRB 080916C, the first bright long burst observed by both instruments, indicated that a Band function provided good representation of the burst spectrum over the full 8 keV–200 GeV energy range (Abdo et al. 2009).

The challenges of untangling the origins of the prompt GRB emission from the prompt gamma-rays alone are long-standing. New observations of higher energy gamma-rays by *Fermi*-LAT, of simultaneous long-wavelength emission by transient monitoring campaigns, and of gamma-ray polarization by Compton telescopes will enrich our view of the prompt emission and provide new clues to its origin.

6. Acknowledgements

ECB thanks Felix Ryde and Asaf Pe'er for useful discussions at the 2008 Huntsville GRB Symposium. He is also grateful to Claudia Wigger and Mark Bandstra for assistance in developing these analysis methods and for comments on a draft of this work.

Facilities: RHESSI

REFERENCES

Abdo, A. A., Ackermann, M., Arimoto, M., Asano, K., Atwood, W. B., Axelsson, M., Baldini, L., Ballet, J., et al. 2009, Science, 323, 1688

Band, D., Matteson, J., Ford, L., Schaefer, B., Palmer, D., Teegarden, B., Cline, T., Briggs, M., et al. 1993, ApJ, 413, 281

Bellm, E. C., Bandstra, M. E., Boggs, S. E., Hajdas, W., Hurley, K., Smith, D. M., & Wigger, C. 2008, in American Institute of Physics Conference Series, Vol. 1000, American Institute of Physics Conference Series, 154–157

Crider, A., Liang, E. P., Smith, I. A., Preece, R. D., Briggs, M. S., Pendleton, G. N., Paciesas, W. S., Band, D. L., et al. 1997, ApJ, 479, L39

Foley, S., McGlynn, S., Hanlon, L., McBreen, S., & McBreen, B. 2008, A&A, 484, 143

Ford, L. A., Band, D. L., Matteson, J. L., Briggs, M. S., Pendleton, G. N., Preece, R. D., Paciesas, W. S., Teegarden, B. J., et al. 1995, ApJ, 439, 307

Ghirlanda, G., Bosnjak, Z., Ghisellini, G., Tavecchio, F., & Firmani, C. 2007, MNRAS, 379, 73

Ghirlanda, G., Celotti, A., & Ghisellini, G. 2002, A&A, 393, 409

—. 2003, A&A, 406, 879

Houck, J. C., & Denicola, L. A. 2000, in Astronomical Society of the Pacific Conference Series, Vol. 216, Astronomical Data Analysis Software and Systems IX, ed. N. Manset, C. Veillet, & D. Crabtree, 591

Kaneko, Y., Preece, R. D., Briggs, M. S., Paciesas, W. S., Meegan, C. A., & Band, D. L. 2006, ApJS, 166, 298

Lin, R. P., Dennis, B. R., Hurford, G. J., Smith, D. M., Zehnder, A., Harvey, P. R., Curtis, D. W., Pankow, D., et al. 2002, Sol. Phys., 210, 3

McBreen, S., Hanlon, L., McGlynn, S., McBreen, B., Foley, S., Preece, R., von Kienlin, A., & Williams, O. R. 2006, A&A, 455, 433

Mészáros, P., & Rees, M. J. 2000, ApJ, 530, 292

Pe'er, A., Ryde, F., Wijers, R. A. M. J., Mészáros, P., & Rees, M. J. 2007, ApJ, 664, L1

Pélangeon, A., Atteia, J.-L., Nakagawa, Y. E., Hurley, K., Yoshida, A., Vanderspek, R., Suzuki, M., Kawai, N., et al. 2008, A&A, 491, 157

Preece, R. D. 2000, in Bulletin of the American Astronomical Society, Vol. 32, Bulletin of the American Astronomical Society, 1231

Preece, R. D., Briggs, M. S., Giblin, T. W., Mallozzi, R. S., Pendleton, G. N., Paciesas, W. S., & Band, D. L. 2002, ApJ, 581, 1248

Preece, R. D., Briggs, M. S., Mallozzi, R. S., Pendleton, G. N., Paciesas, W. S., & Band, D. L. 1998a, ApJ, 506, L23

Preece, R. D., Pendleton, G. N., Briggs, M. S., Mallozzi, R. S., Paciesas, W. S., Band, D. L., Matteson, J. L., & Meegan, C. A. 1998b, ApJ, 496, 849

Protassov, R., van Dyk, D. A., Connors, A., Kashyap, V. L., & Siemiginowska, A. 2002, ApJ, 571, 545

Ryde, F. 2004, ApJ, 614, 827

—. 2005, ApJ, 625, L95

Ryde, F., Björnsson, C.-I., Kaneko, Y., Mészáros, P., Preece, R., & Battelino, M. 2006, ApJ, 652, 1400

Ryde, F., & Pe'er, A. 2008, ApJ, submitted (arXiv: 0811.4135)

Sakamoto, T., Lamb, D. Q., Kawai, N., Yoshida, A., Graziani, C., Fenimore, E. E., Donaghy, T. Q., Matsuoka, M., et al. 2005, ApJ, 629, 311

Scargle, J. D. 1998, ApJ, 504, 405

Smith, D. M., Lin, R. P., Turin, P., Curtis, D. W., Primbsch, J. H., Campbell, R. D., Abiad, R., Schroeder, P., et al. 2002, Sol. Phys., 210, 33

Sturner, S. J., Seifert, H., Shrader, C., & Teegarden, B. J. 2000, in American Institute of Physics Conference Series, Vol. 510, American Institute of Physics Conference Series, ed. M. L. McConnell & J. M. Ryan, 814

Vanderspek, R., Sakamoto, T., Barraud, C., Tamagawa, T., Graziani, C., Suzuki, M., Shirasaki, Y., Prigozhin, G., et al. 2004, ApJ, 617, 1251

Wigger, C., Wigger, O., Bellm, E., & Hajdas, W. 2008, ApJ, 675, 553

This preprint was prepared with the AAS LaTeX macros v5.2.

Table 1. Intervals used for spectral fitting. The intervals are quoted relative to the start time T_0.

GRB	Off-Axis Angle	T_0 (UT)	Interval Edges (sec)
		High S/N Sample	
020715	72°	19:21:08.666	0.000, 0.356, 0.646, 3.336
021008A	50°	07:01:01.399	0.000, 1.265, 1.985, 2.541, 2.727, 2.934, 3.142, 3.278, 3.542, 3.889, 4.054, 4.314, 4.438, 4.995, 8.153, 8.617
021206	18°	22:49:12.951	0.000, 1.983, 2.163, 2.267, 2.405, 2.626, 3.012, 3.176, 3.377, 3.487, 3.559, 3.629, 3.714, 3.809, 3.871, 3.959, 4.024, 4.099, 4.361, 4.618, 4.699, 4.792, 4.945, 5.068, 5.168, 5.346, 5.552, 5.718, 6.112, 6.217, 6.603, 6.906
030329A	144°	11:37:25.954	0.000, 2.266, 2.833, 3.520, 3.979, 4.351, 5.019, 6.226, 13.431, 14.335, 15.006, 15.687, 17.553
030519B	166°	14:04:52.951	0.000, 5.769, 6.352, 6.726, 7.027, 7.214, 7.625, 11.065
031027	102°	17:07:37.744	0.000, 3.236, 4.774, 6.065, 9.469
031111	156°	16:45:20.776	0.000, 0.329, 0.971, 1.329
040228	163°	00:08:50.910	0.000, 4.751, 6.291, 8.458, 13.995, 15.009, 17.221, 17.563, 18.338, 22.981, 27.748
040810	144°	14:16:40.241	0.000, 17.055, 24.995, 45.637
		Single-Pulse Sample	
020715	72°	19:21:07.907	0.000, 0.543, 0.759, 1.115, 1.236, 1.397, 1.521, 1.810, 5.135
030329A	144°	11:37:25.954	0.000, 2.280, 2.895, 3.356, 3.997, 4.355, 5.020, 5.287, 5.743, 6.287, 7.529, 9.616, 13.523
060805B	97°	14:27:15.989	0.000, 1.245, 1.632, 2.537, 3.428, 4.451

Table 2. Comparison of time-integrated Band fit parameters for bursts fit in other works. Results of the closest analagous fit are shown. Only the limits of the RHESSI fit energy band are presented when different ranges were used for the front and rear segments. Parameter uncertainties have been converted to 90% C.L. where necessary.

GRB	Instrument	Fit Band	α	E_{peak}(keV)	β	χ^2/dof	Reference
020715	RHESSI	30 keV–17 MeV	$-0.71^{+0.11}_{-0.10}$	477^{+59}_{-52}	$-2.79^{+0.24}_{-0.50}$	34.5/26	(1)
	RHESSI	30 keV–15.7 MeV	-0.776±0.072	531±39	-3.14±0.41	106.3/113	(2)
021008A	RHESSI	100 keV–17 MeV	$-1.360^{+0.035}_{-0.034}$	733^{+16}_{-16}	$-3.59^{+0.11}_{-0.14}$	59.7/30	(1)
	RHESSI	300 keV–15.7 MeV	-1.493±0.092	677±54	-3.73±0.30	79.5/84	(2)
021206	RHESSI	30 keV–17 MeV	$-0.817^{+0.031}_{-0.030}$	718^{+17}_{-17}	$-2.912^{+0.053}_{-0.059}$	118/68	(1)
	RHESSI	70 keV–4.5 MeV	-0.692±0.033	711±12	-3.19±0.07	176.5/174	(2)
030329A	RHESSI	30 keV–17 MeV	$-1.648^{+0.060}_{-0.053}$	139^{+7}_{-7}	$-3.03^{+0.24}_{-0.53}$	101.4/46	(1)
	RHESSI (peak 1)	34 keV–10 MeV	-1.608±0.063	157.2±8.6	-3.48±0.87	84.3/90	(2)
	RHESSI (peak 2)	34 keV–7 MeV	-1.78±0.11	85±18	-3.04±0.49	103.3/83	(2)
	HETE	2 keV–400 keV	-1.32±0.02	70.2±2.3	-2.44±0.08	···	(3)
	HETE	2 keV–400 keV	$-1.26^{+0.01}_{-0.02}$	68±2	$-2.28^{+0.05}_{-0.06}$	213.7/139	(4)
030519B	RHESSI	50 keV–17 MeV	$-1.171^{+0.049}_{-0.046}$	437^{+23}_{-22}	$-3.11^{+0.23}_{-0.40}$	66/35	(1)
	RHESSI	70 keV–15 MeV	-1.048±0.069	417.2±21	-3.11±0.30	86.3/75	(2)
	HETE	2 keV–400 keV	-0.8±0.1	138^{+18}_{-15}	-1.7±0.2	92.0/124	(4)
031027	RHESSI	30 keV–17 MeV	$-0.759^{+0.089}_{-0.080}$	319^{+26}_{-24}	< -2.79	63.9/56	(1)
	RHESSI	60 keV–6 MeV	-0.94±0.13	338±25	···	···	(2)
031111	RHESSI	30 keV–17 MeV	$-1.071^{+0.073}_{-0.061}$	841^{+96}_{-89}	$-2.83^{+0.22}_{-0.38}$	50.2/56	(1)
	RHESSI	38 keV–15.7 MeV	-1.102±0.059	844±97	-2.364±0.11	128.3/117	(2)
	HETE	2 keV–400 keV	$-0.82^{+0.05}_{-0.5}$	404^{+68}_{-51}	···	···	(5)
040228	RHESSI	50 keV–17 MeV	$-1.60^{+0.037}_{-0.034}$	769^{+120}_{-99}	$-2.50^{+0.18}_{-0.36}$	107.9/84	(1)
040810	RHESSI	30 keV–17 MeV	$-1.45^{+0.12}_{-0.10}$	321^{+50}_{-45}	< -2.52	55.7/56	(1)

Note. — (1) This work (2) Wigger et al. (2008) (3) Vanderspek et al. (2004) (4) Sakamoto et al. (2005) (5) Pélangeon et al. (2008)

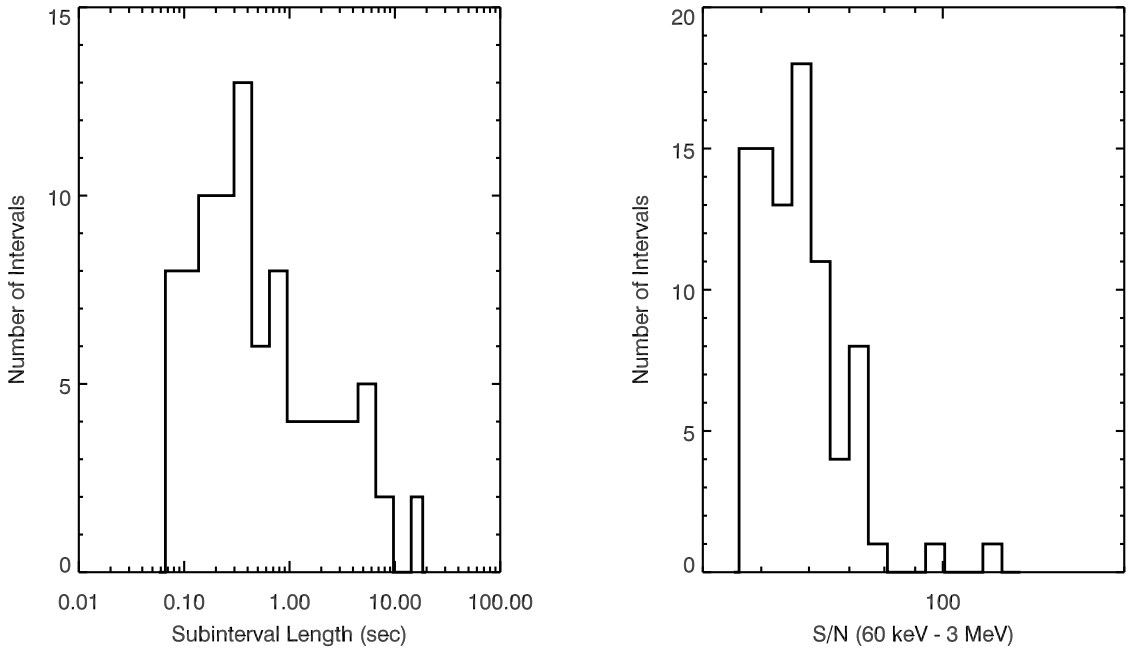

Fig. 1.— Distribution of subinterval length and signal-to-noise ratio for the high S/N burst sample considered in this work.

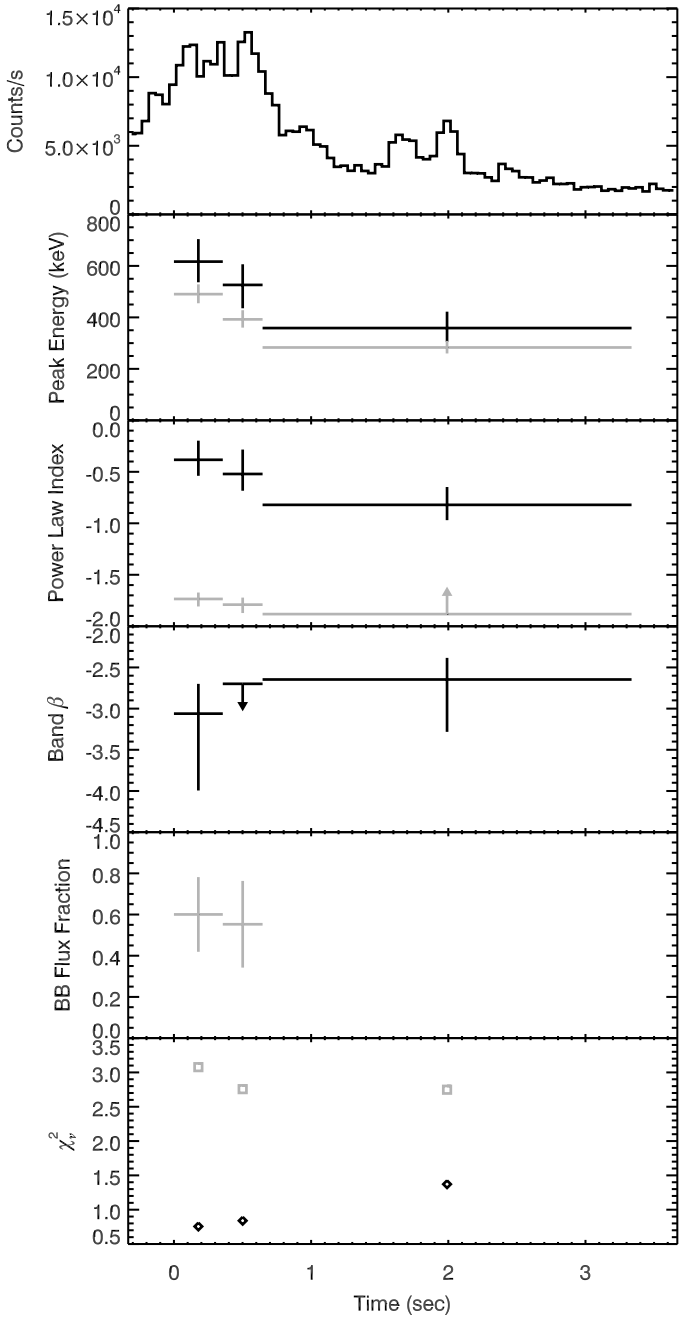

Fig. 2.— Spectral evolution of GRB 020715. The 60 keV–3 MeV lightcurve has 0.05 s time bins; counts are shown only for those segments used in the fits. The fit model parameters are black for the Band model and gray for the BBPL model. All errors are 90% C.L. Peak energies are E_{peak} for the Band model and 3.92 kT for the BBPL model. The Band model α is plotted with the power-law index s of the BBPL model. The errors on the fraction of the flux provided by the black body in the RHESSI band were estimated from a Monte Carlo bootstrap. Points where the value was unconstrained in the fit are omitted from the plot.

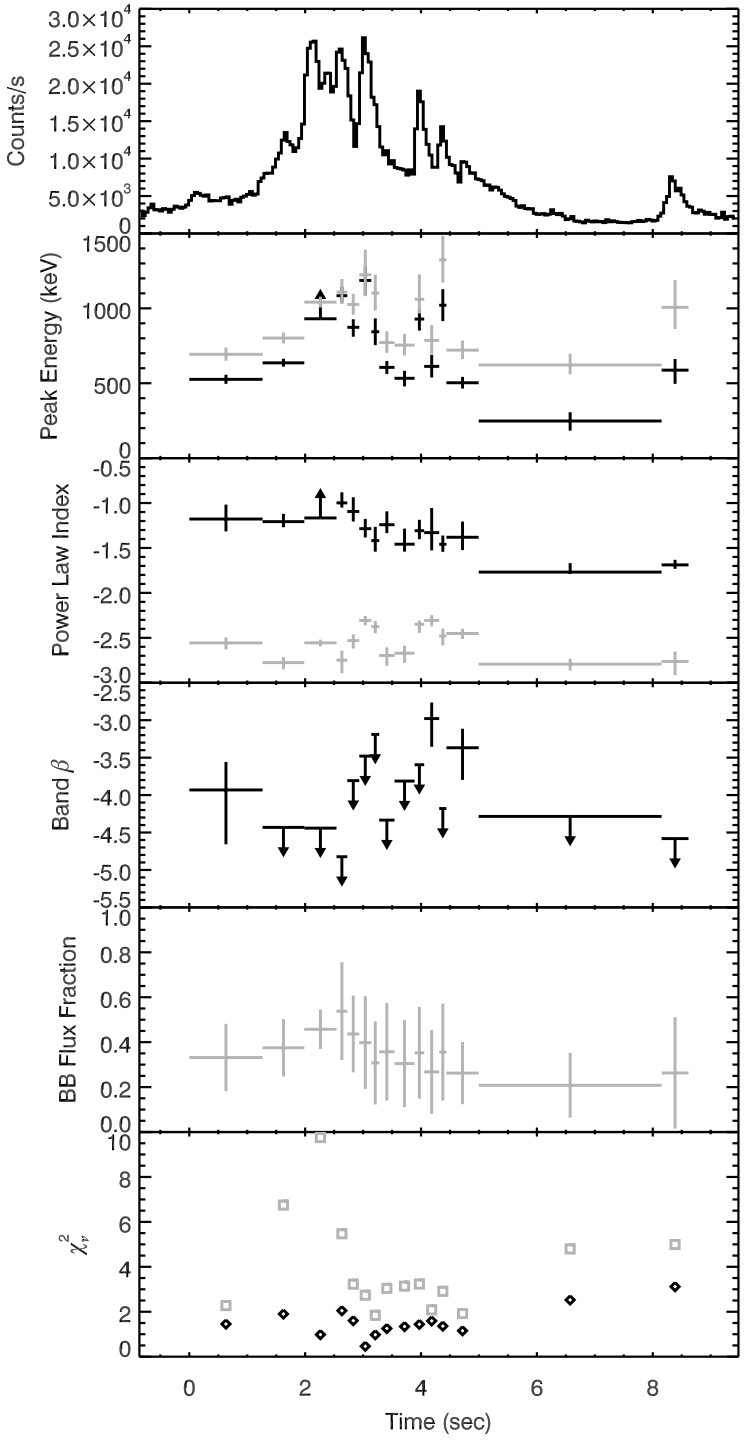

Fig. 3.— Spectral evolution of GRB 021008A. Symbols as in Fig. 2.

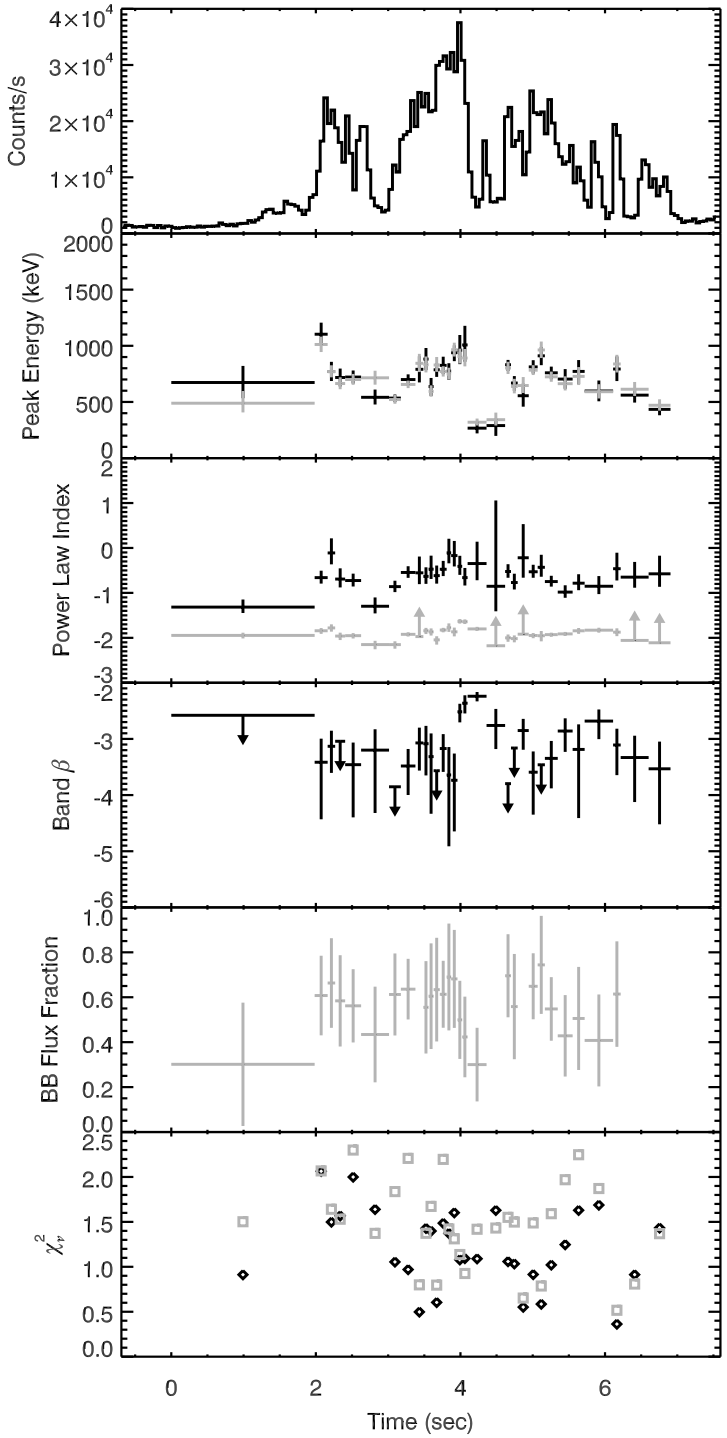

Fig. 4.— Spectral evolution of GRB 021206. Symbols as in Fig. 2.

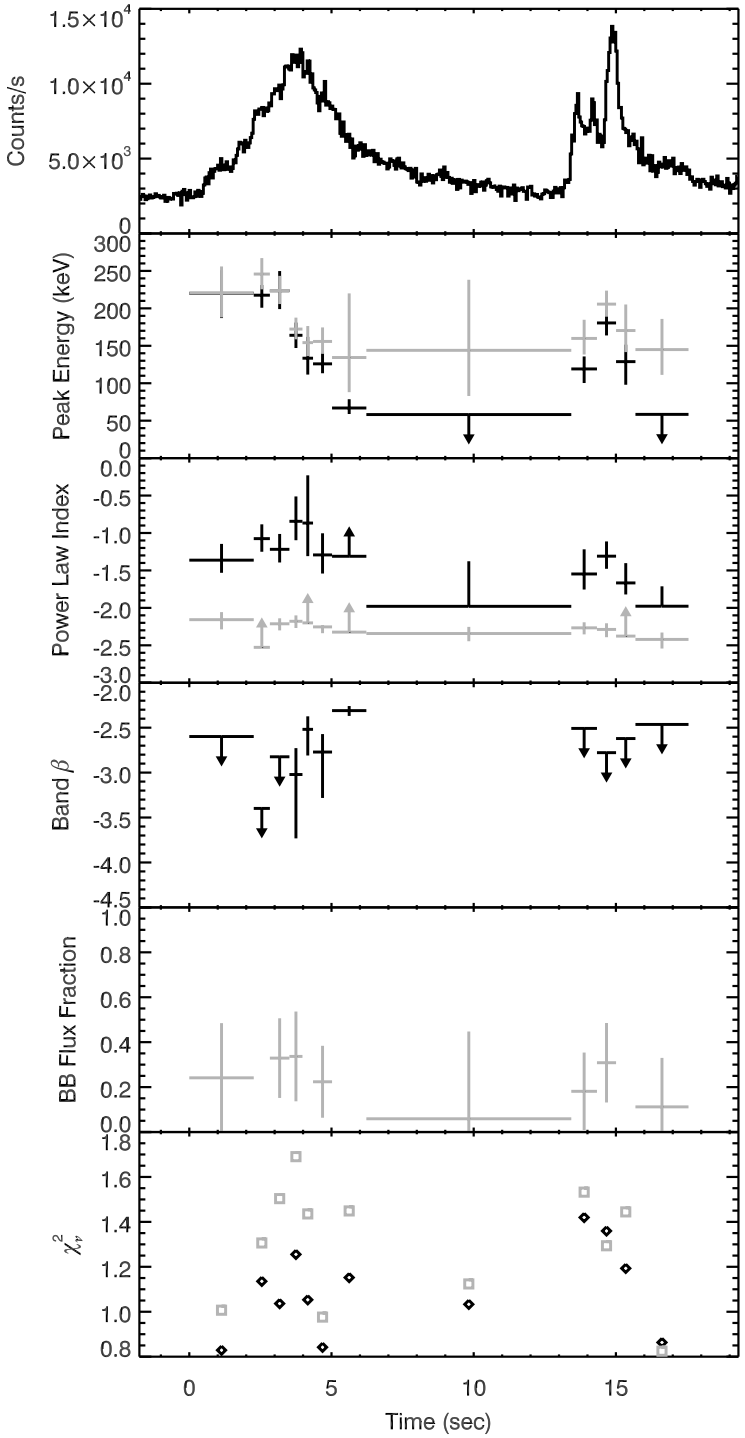

Fig. 5.— Spectral evolution of GRB 030329. Symbols as in Fig. 2.

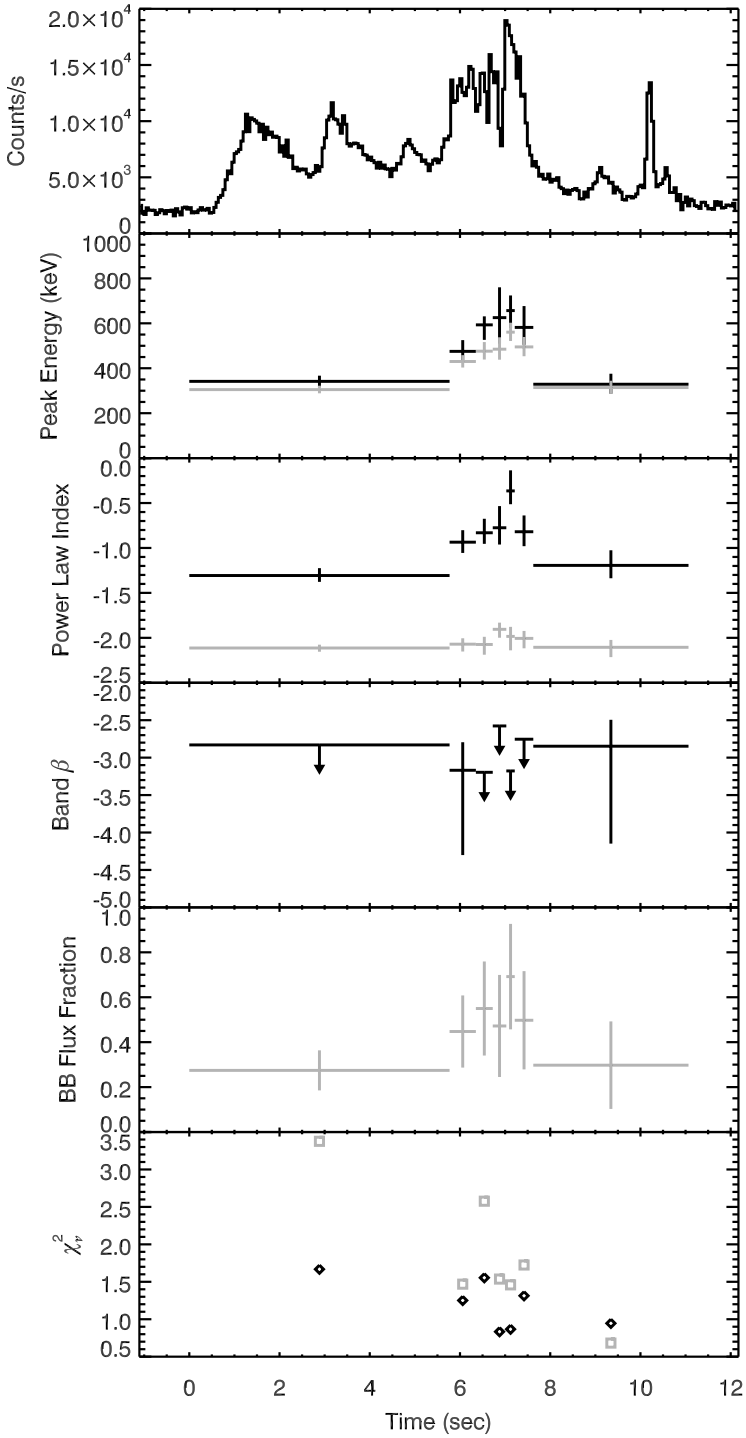

Fig. 6.— Spectral evolution of GRB 030519. Symbols as in Fig. 2.

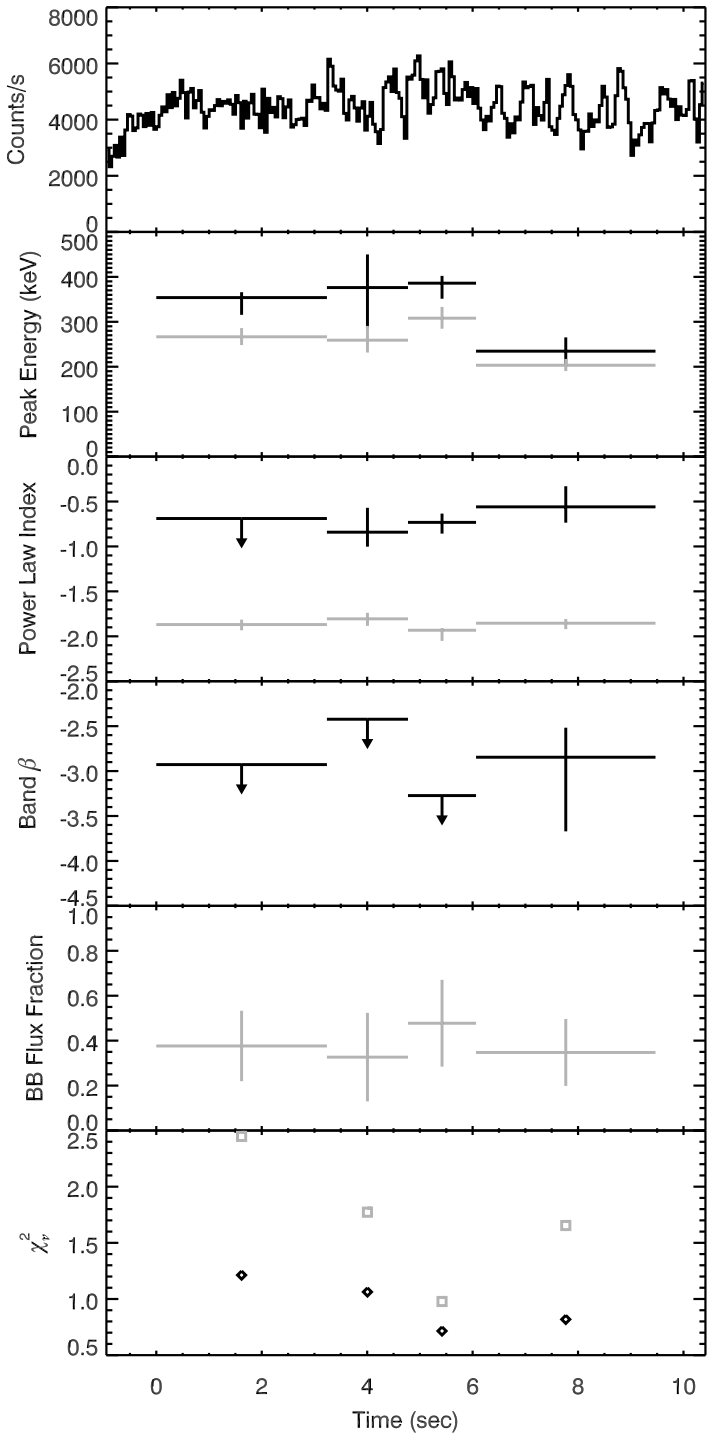

Fig. 7.— Spectral evolution of GRB 031027. Symbols as in Fig. 2. The lightcurve appears flat because the background level is not visible in the time interval plotted.

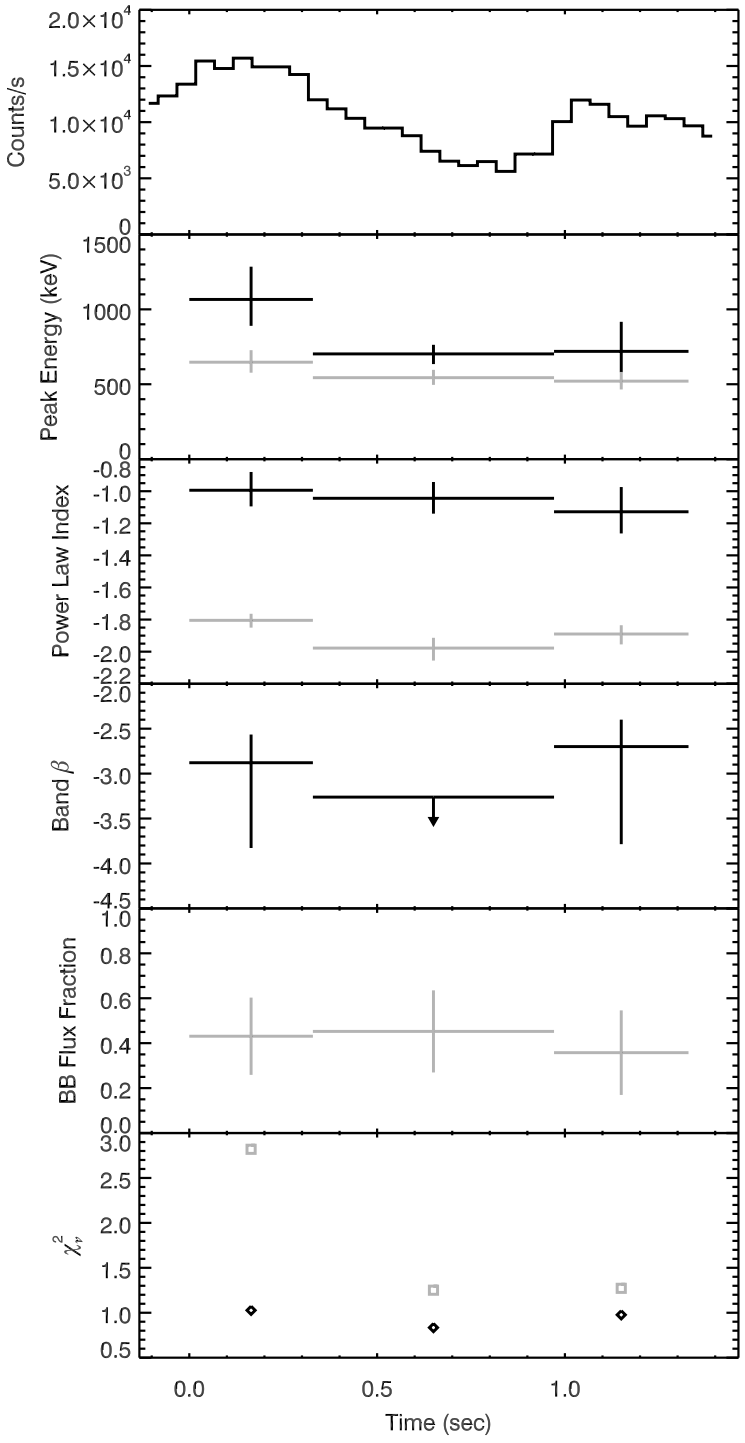

Fig. 8.— Spectral evolution of GRB 031111. Symbols as in Fig. 2.

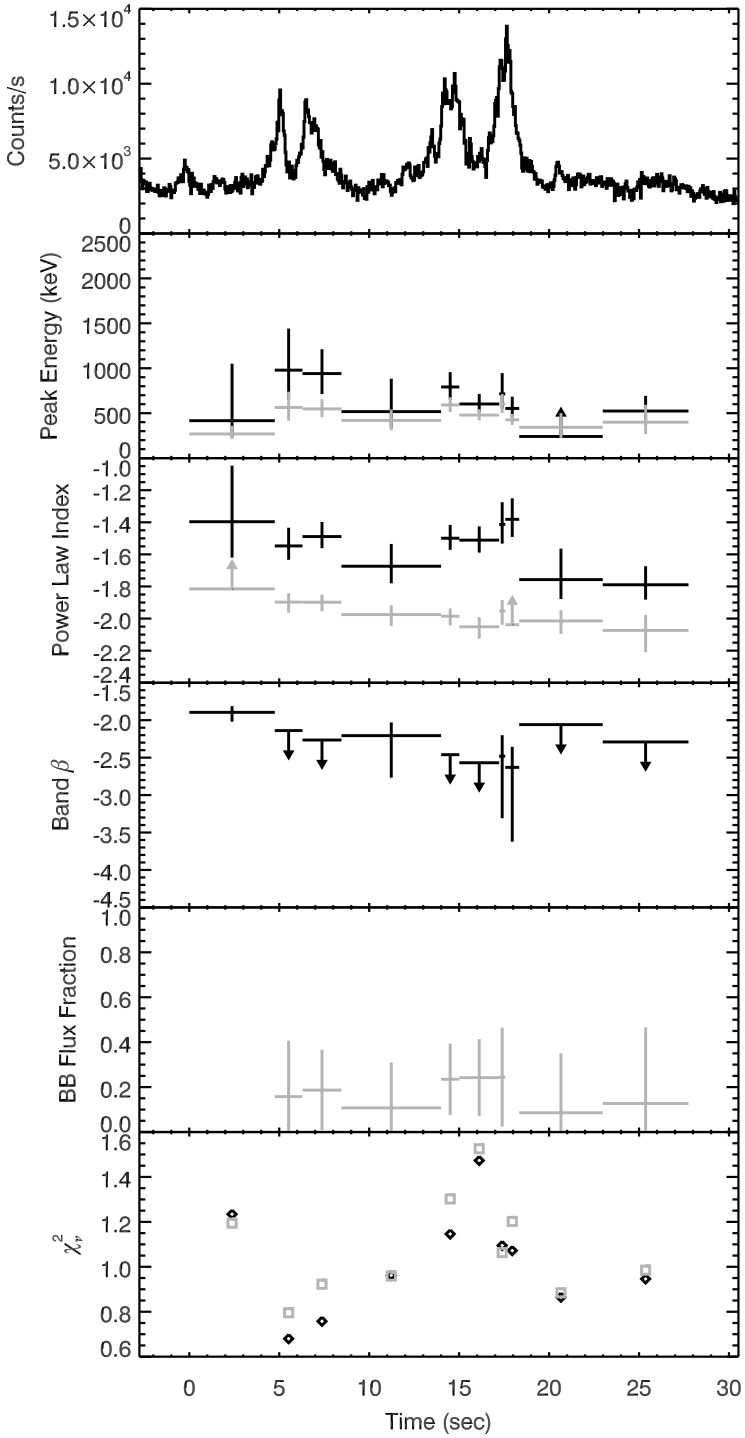

Fig. 9.— Spectral evolution of GRB 040228. Symbols as in Fig. 2.

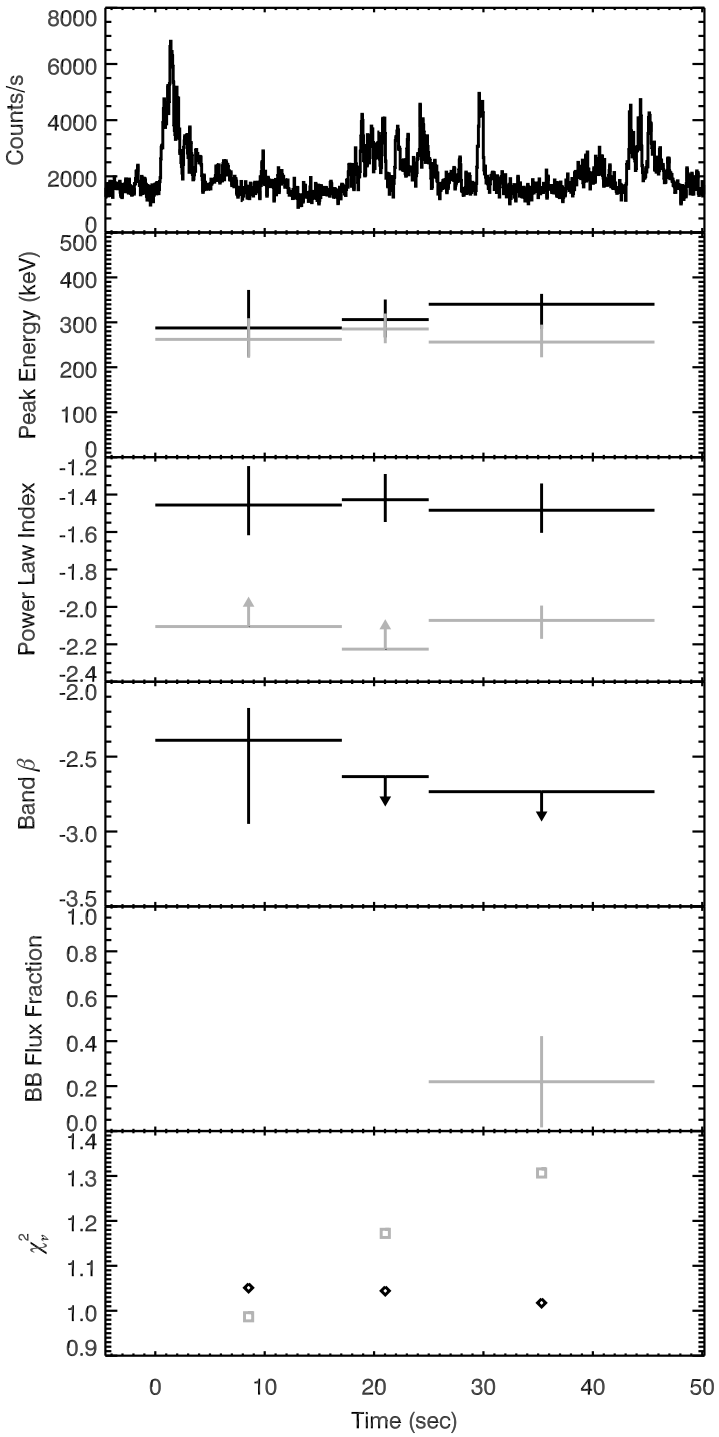

Fig. 10.— Spectral evolution of GRB 040810. Symbols as in Fig. 2.

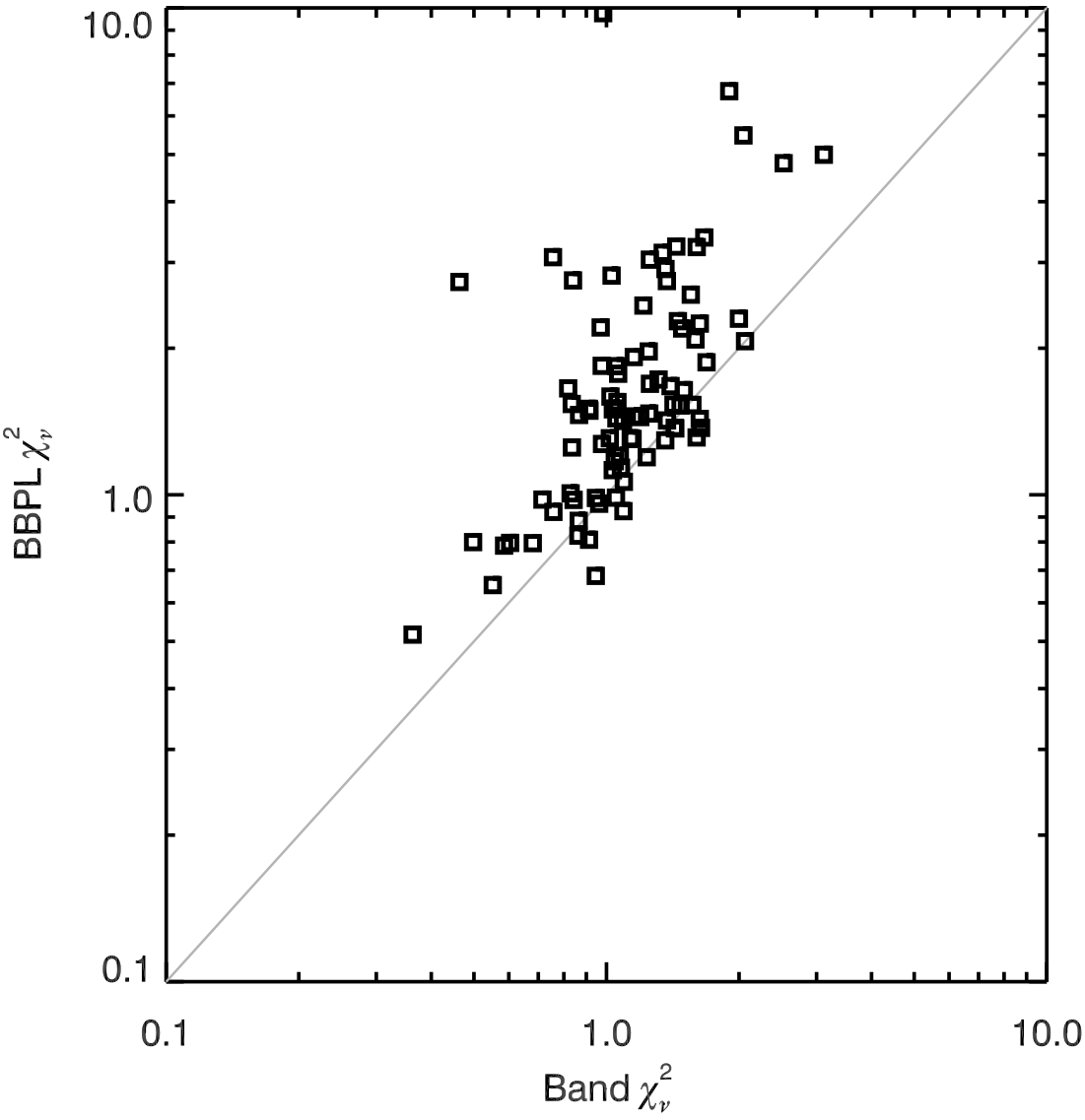

Fig. 11.— Comparison of the reduced chi-squared values for fits to the Band and BBPL models, which have identical degrees of freedom. The Band model is generally preferred.

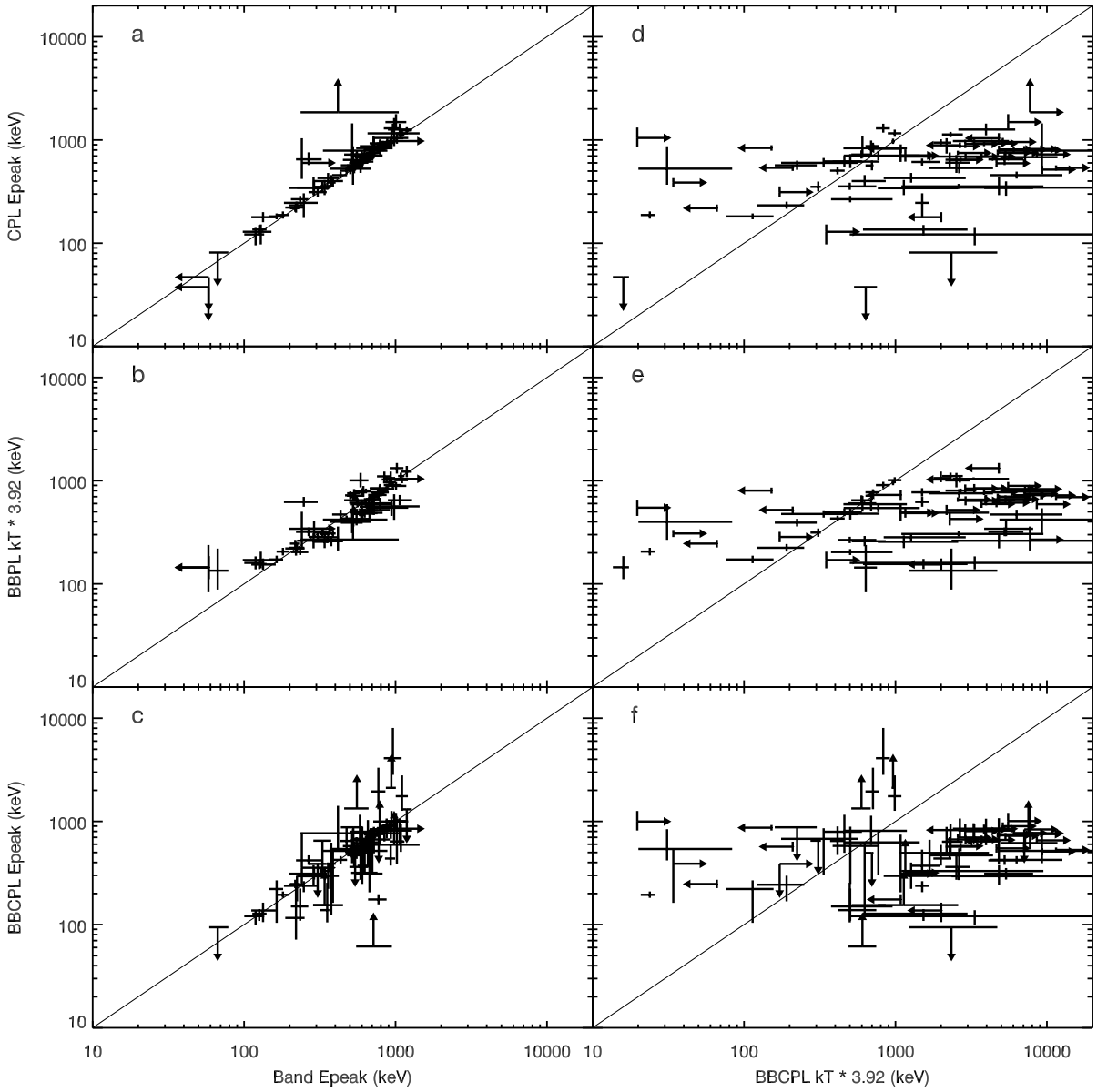

Fig. 12.— Comparison of peak energies obtained in Band, CPL, BBPL, and BBCPL fits. As expected, there is good agreement between the E_{peak} values of the Band and CPL models (panel a). Notably, the black-body peak (3.92 kT) of the BBPL model and the BBCPL E_{peak} parameter also match the Band function E_{peak} (panels b and c). However, the black-body peak of the BBCPL model shows little correlation with the spectral peak identified by the other models (panels d–f). A few points which were completely unconstrained in one dimension are omitted in the plot.

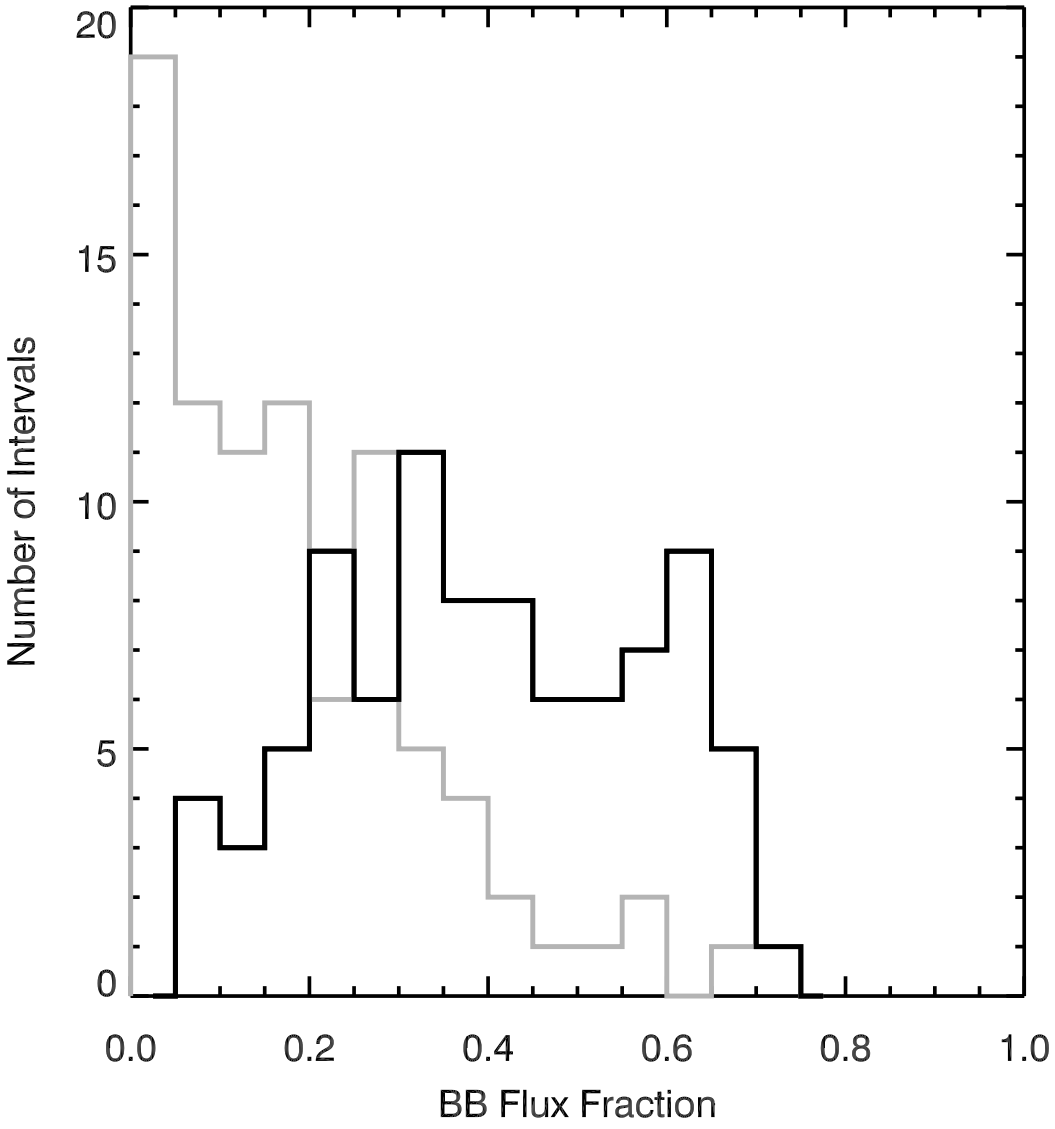

Fig. 13.— Histogram of the proportion of flux in the RHESSI band contributed by the blackbody component in the BBPL (black) and BBCPL (gray) models. With the nonthermal component providing the spectral break in the BBCPL model, the relevance of the black body component diminishes.

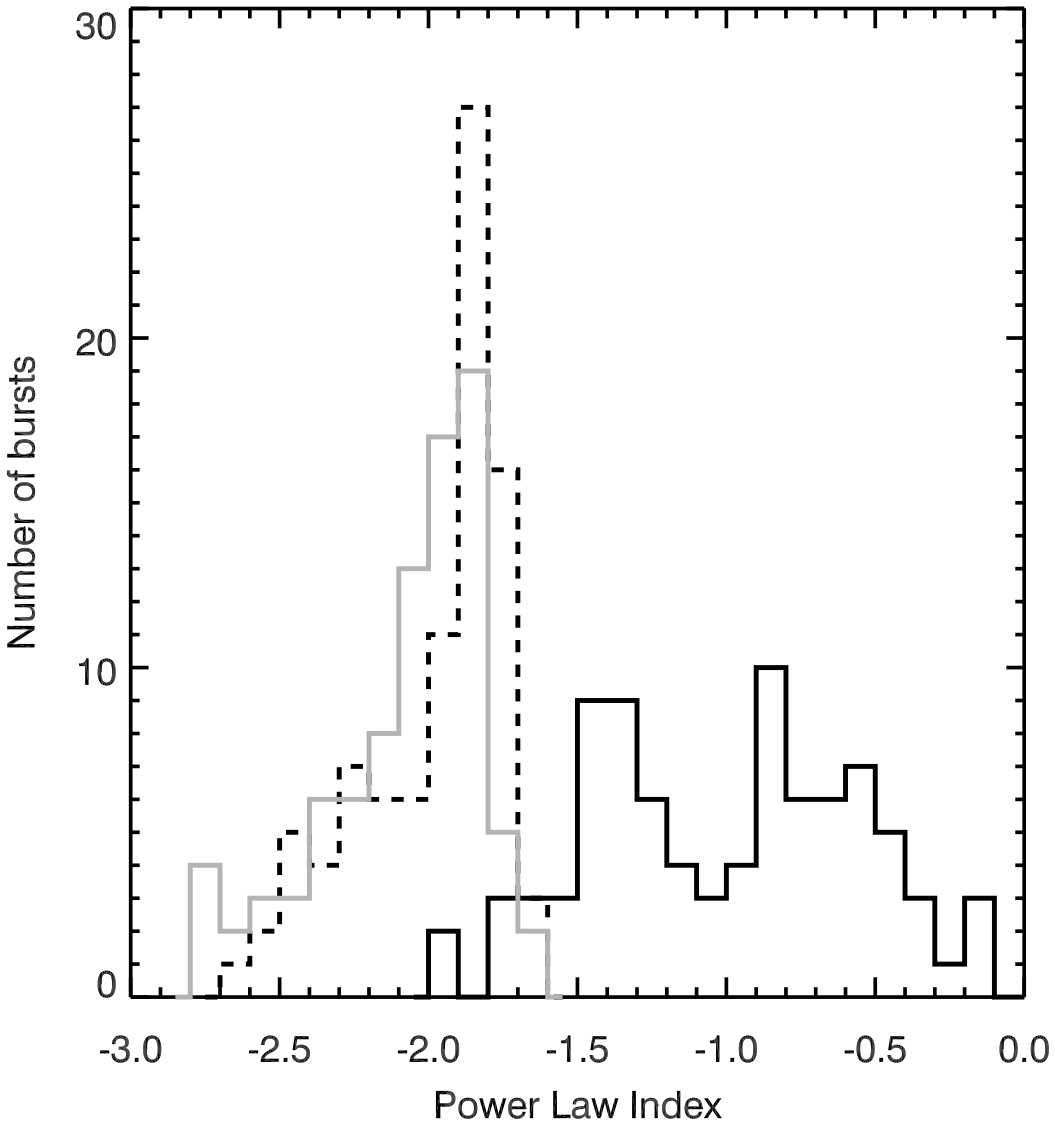

Fig. 14.— Histogram of the fit low-energy power law indices for the Band model (solid black), BBPL model (solid gray), and simple power-law model (dashed black). The indices of the PL model and the BBPL model are highly correlated. The apparent bimodality of the Band α index is likely an artifact of the limited burst sample (Section 3).

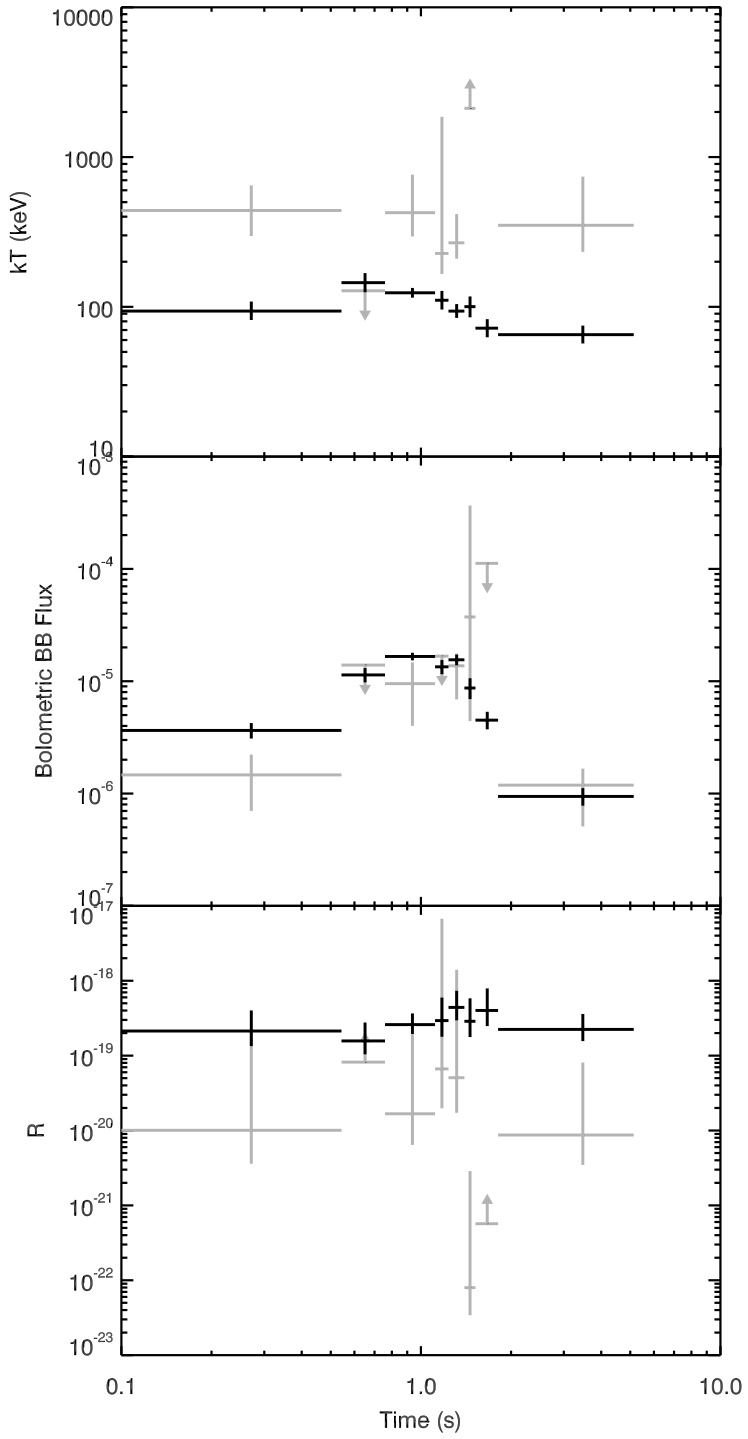

Fig. 15.— Time evolution of the temperature, black-body flux, and $\mathcal{R}$ for the single-pulse burst GRB 020715. BBPL model fits are black, while BBCPL fits are gray.

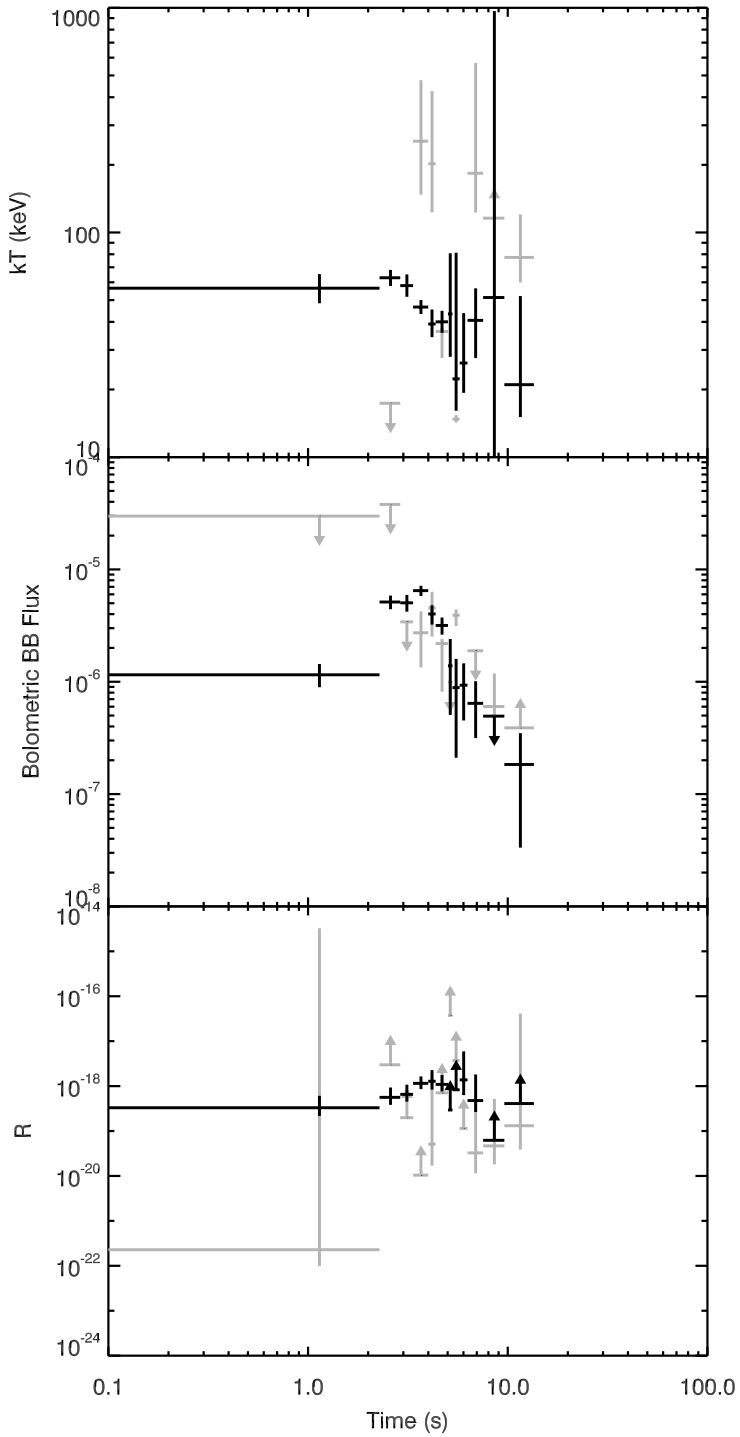

Fig. 16.— Data for the single-pulse burst GRB 030329. Symbols as in Fig. 15.

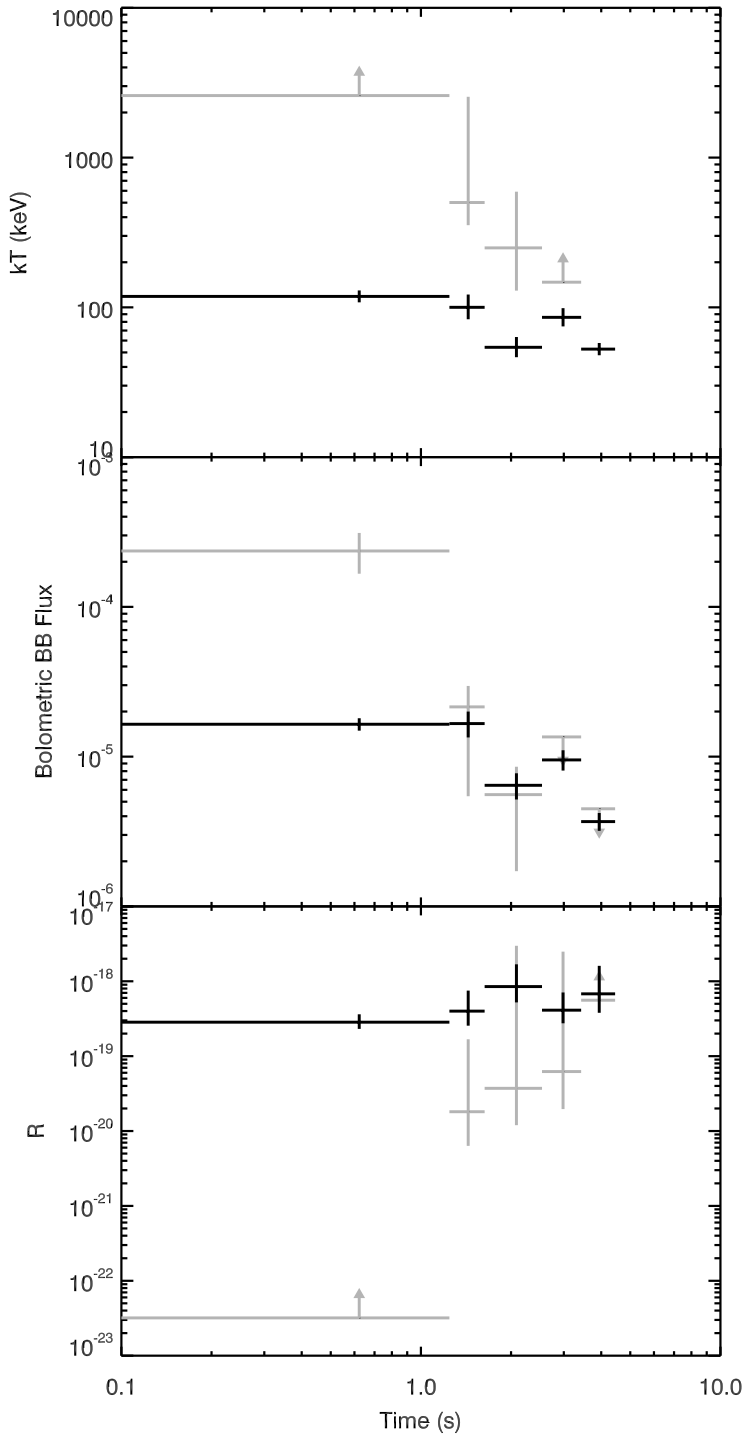

Fig. 17.— Data for the single-pulse burst GRB 060805. Symbols as in Fig. 15.